(Preprint) AAS 08-XXX

CRATER IDENTIFICATION ALGORITHM FOR THE LOST IN LOW LUNAR ORBIT SCENARIO

Dr. Chad Hanak[*], Dr. Tim Crain[†], and Dr. Robert Bishop[‡]

Recent emphasis by NASA on returning astronauts to the Moon has placed attention on the subject of lunar surface feature tracking. Although many algorithms have been proposed for lunar surface feature tracking navigation, much less attention has been paid to the issue of navigational state initialization from lunar craters in a lost in low lunar orbit (LLO) scenario. That is, a scenario in which lunar surface feature tracking must begin, but current navigation state knowledge is either unavailable or too poor to initiate a tracking algorithm. The situation is analogous to the lost in space scenario for star trackers. A new crater identification algorithm is developed herein that allows for navigation state initialization from as few as one image of the lunar surface with no a priori state knowledge. The algorithm takes as inputs the locations and diameters of craters that have been detected in an image, and uses the information to match the craters to entries in the USGS lunar crater catalog via non-dimensional crater triangle parameters. Due to the large number of uncataloged craters that exist on the lunar surface, a probability-based check was developed to reject false identifications. The algorithm was tested on craters detected in four revolutions of Apollo 16 LLO images, and shown to perform well.

INTRODUCTION

With a renewed interest in returning astronauts to the Moon, attention is returning to the subject of on-board lunar surface feature tracking. This capability would provide NASA's Orion vehicle with the capability to generate an on-board navigational state sufficient to return its crew to Earth in the event that communication is lost with Earth-based tracking assets. Many studies have reported on the adequacy of lunar landmark tracking navigation for the purpose of Earth return. However, less attention has been directed to the problem of navigational state initialization.

Before lunar landmark tracking can begin, the on-board navigation system must be able to localize the spacecraft with respect to the surface so that the landmark tracking subsystem knows approximately where to locate known surface features. The localization process can be performed in two ways: 1) the current navigation state estimate can be used, or 2) a navigation state reinitialization can be done using information available from on-board sensors. In the former case, the current navigation state estimate may be unavailable (hence "lost in space") or severely degraded. The likelihood of success for the landmark tracking subsystem in this situation would be poor at best. Developing the latter capability using on-board sensors yields a more robust landmark tracking subsystem, especially in the event that the current navigation state estimate is unavailable. Just as many star trackers have separate tracking and lost in space initialization algorithms, it is prudent

[*]GN&C Autonomous Flight Systems Branch (EG6), Aeroscience and Flight Mechanics Division, NASA - Johnson Space Center, 2101 NASA Parkway, Houston, TX 77058 (email: chad.hanak-1@nasa.gov).

[†]GN&C Autonomous Flight Systems Branch (EG6), Aeroscience and Flight Mechanics Division, NASA - Johnson Space Center, 2101 NASA Parkway, Houston, TX 77058.

[‡]Department of Aerospace Engineering and Engineering Mechanics, Cockrell School of Engineering, The University of Texas at Austin, 210 E. 24th St., WRW 318B, 1 University Station, C0600, Austin, TX 78712.

for spacecraft operating in lunar orbit to have a lost in low lunar orbit (LLO) state initialization algorithm, in addition to a lunar landmark tracking algorithm.

The core of a lost in LLO navigation state initialization algorithm would be comprised of crater detection and identification algorithms that can function without *a priori* state knowledge. The crater identification algorithm is the focus of this paper, while the crater detection algorithm, which finds craters within an image, is assumed to be a given (see[1] for a description of the crater detection algorithm). Once craters are detected in an image and their locations and radii estimated, those values are sent to the crater identification algorithm. The existing literature on the subject of crater identification is presented in[2] and,[3] however, the lost in low lunar orbit scenario is not addressed in either, and the algorithms differ significantly from that developed in this paper.

CRATER PATTERN MATCHING STRATEGY

Geometric patterns involving multiple craters are used for crater identification in this paper to avoid the drawbacks of image correlation techniques. These include large storage and processing requirements and difficulties in dealing with the effects of unknown shadowing, unknown altitude (scale), and unknown roll orientation about the nadir vector (recall that this is a lost in LLO algorithm). In contrast, matching geometric patterns involving the craters within the image only requires information about relative crater locations and diameters, measurements of which are readily available from a crater detection algorithm that can operate efficiently under a wide range of crater shadowing, scale uncertainty, and with unknown roll orientation about nadir.[1] Additionally, values of these parameters are available in the USGS lunar crater database[4] for each cataloged crater.

Due to the lack of accurate altitude knowledge in a lost in LLO scenario, only non-dimensional geometrical parameters can be used for crater identification. Previous research involving non-dimensional star identification algorithms have utilized star triangles for identification, as the angles of the triangle projected onto the image plane are independent of the triangle scale.[5] Such a method can also be used for crater identification because the scale of the planar crater triangles will vary with altitude, but the angles will not.

Figure 1 depicts an image of a typical crater triangle, with the smallest and largest angles denoted as α_s and α_l, respectively. Only the smallest and largest angles of the triangle are used since the remaining angle can be calculated by subtracting the other two from 180 degrees.

In most images, the accuracy of the measured crater triangle angles, as compared to the crater triangle angles computed from the USGS lunar crater database,[4] are not accurate enough to uniquely identify a crater pattern from less than 5 or 6 craters. As a result, several secondary, less accurate identifiers are also used.

Non-dimensional crater diameter ratios, calculated as the ratio of a crater diameter to the longest leg of its corresponding crater triangle, are used as secondary identifiers. In Figure 1, the measured diameters of craters i, j, and k would be divided by the length of $\boldsymbol{r}_{ij}$, all in pixels, to get the crater diameter ratios.

The sense of rotation of a crater triangle is also used, as it allows for discrimination between the triangle and its mirror image, as viewed from above. Tracing the triangle from the vertex of its smallest angle, to that of its middle angle, and then its largest angle, will result in either a clockwise or counter-clockwise path. For instance, in Figure 1, a counter-clockwise path is traced out as one proceeds from the vertex of the smallest angle (i), to the vertex of the middle angle (j), to the vertex of the largest angle (k).

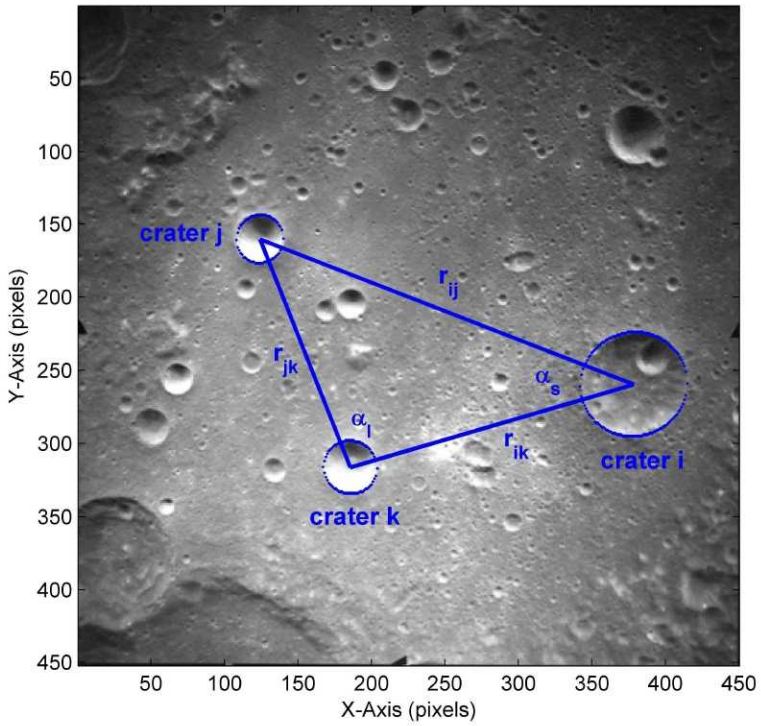

Figure 1 Crater Triangle Formed With 3 Craters in Apollo 16 Lunar Surface Image AS16-M-0060;[6] Smallest and Largest Angles of the Triangle are Denoted as α_s and α_l, Respectively

The basic crater pattern matching strategy is to select two reference craters from the list of detected craters in the image provided by the crater detection algorithm. Then a third crater is selected to form a crater triangle with the two reference craters. For illustrative purposes, the reference craters are craters i and j in Figure 1, and the third crater is crater k. The cosines of the smallest and largest angles of the triangle (α_s and α_l in Figure 1, respectively), the crater diameter ratios, and the sense of triangle rotation are all then calculated and the crater triangle list (prepared ahead of time from the USGS lunar crater database) is searched for cataloged crater triangles that match the measurements to within computed tolerances. There will generally be multiple cataloged triangles that match the imaged triangle to within tolerances. In a similar manner, crater triangles are formed between the two reference craters and the remaining craters, and lists of crater triangles that match the measured angle cosines, diameter ratios, and sense of rotation to within tolerances are created. For instance, there is only 1 remaining crater with a radius between 11 km and 42 km in Figure 1, and the triangle that is formed between it and the reference craters is depicted in Figure 2. Then each of the resulting crater triangle lists is compared with the others to find entries that have matching names for the reference craters i and j. An identification is made when one pair of reference crater names appears more than any other. In that sense, there is only one unique match in the crater database for the observed crater pattern. The probability that said match is a false identification is then computed, and those with a high probability of being incorrect are rejected as a way to ensure robustness against detected craters that are not actually in the USGS lunar crater database (there are many of these uncataloged craters). If a unique match is not found, then a new pair of

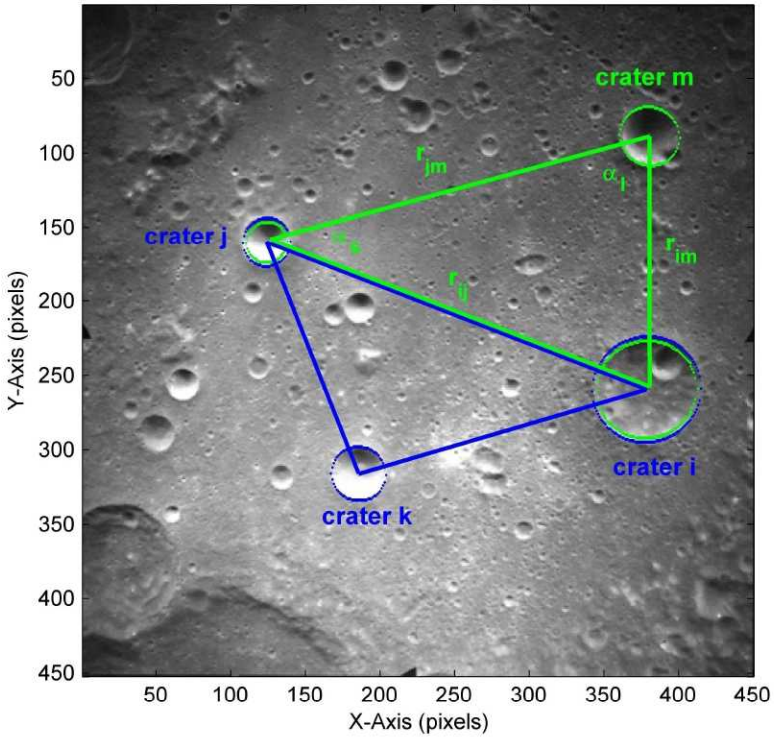

Figure 2 Two Crater Triangles Formed With 4 Craters in Apollo 16 Lunar Surface Image AS16-M-0060;[6] Smallest and Largest Angles of the 2^{nd} Triangle are Denoted as α_s and α_l, Respectively

reference craters is chosen and the process is repeated until all reference crater combinations have been examined.

CRATER TRIANGLE LIST CREATION

The USGS lunar crater database provides the names, latitudes, longitudes, and diameters of 1570 lunar craters and 7103 satellite features (these are small craters surrounding larger craters, and are also known as lettered craters).[4] Thus, the database provides information on 8673 craters (no distinction between craters and satellite features is made here). Of these craters, a crater detection algorithm can reasonably detect craters ranging in diameter from 11 km to 42 km while in low lunar orbit (LLO). Anything smaller than 11 km tends to be dominated by spatial frequency components that are close to those of the rocky lunar terrain, making detection difficult with an automated algorithm. Anything larger that 42 km is ill-defined from the LLO altitudes, and a reasonably well defined crater rim is necessary for good crater detection. Therefore, only the 4117 craters in the USGS database with diameters between 11 km and 42 km were considered.

The crater identification algorithm was designed to identify crater triangles that a crater detection algorithm has found within an image taken from LLO. The smallest and largest angles, three crater diameter ratios, and sense of rotation of each triangle are used for matching purposes. With this in mind, a list had to be be created that contained these parameters for each cataloged crater triangle that could fit within the camera field of view (FOV) while in LLO.

Images from the mapping camera on Apollo 16 were used to test this algorithm, and the FOV for said camera had a half angle of 37 degrees.[6] The altitude range for the Apollo 16 orbits during which these images were taken was 100 km to 124 km. To determine if the crater triangle could be seen in its entirety by the camera, the maximum size of the projection of the camera FOV onto the lunar surface had to be determined. It was be assumed that the FOV was circular and that the diameter was such that it encompassed the actual square FOV. Therefore, using a flat Moon approximation and a maximum assumed altitude of $h_{max} = 124$ km, the diameter of the projection of the camera circular FOV onto the lunar surface was determined to be

$$\begin{aligned} d_{fov} &= 2\sqrt{2}\left(h_{max}\tan(37^\circ)\right) \\ &= 263 \text{ km} \end{aligned} \tag{1}$$

Using this knowledge, the 4117 ideally sized craters in the USGS catalog were searched for combinations of 3 that could fit, crater extents and all, within a 263 km circle. For those that could, the following parameters were calculated and logged:

$$\left[\begin{array}{ccccccccc} i_s & i_m & i_l & \cos\alpha_s & \cos\alpha_l & \gamma_s & \gamma_m & \gamma_l & I_{ccw/cw} \end{array}\right]_{1\times 9} \tag{2}$$

where i_s, i_m, and i_l are the crater identification numbers for the craters at the vertices of the small, medium, and large angles of the triangle, respectively. Using the example of Figure 1, $i_s = i$, $i_m = j$, and $i_l = k$. The crater diameter ratios were calculated according to (using the aforementioned triangle example)

$$\begin{aligned} \gamma_s &= \frac{d_i}{\|\boldsymbol{r}_{ij}\|} \\ \gamma_m &= \frac{d_j}{\|\boldsymbol{r}_{ij}\|} \\ \gamma_l &= \frac{d_k}{\|\boldsymbol{r}_{ij}\|} \end{aligned} \tag{3}$$

where the relative position vectors were defined in terms of the lunar-centric position vector of each crater defined by the latitude and longitude entries in the USGS catalog,

$$\begin{aligned} \boldsymbol{r}_{ij} &= \boldsymbol{r}_j - \boldsymbol{r}_i \\ \boldsymbol{r}_{ik} &= \boldsymbol{r}_k - \boldsymbol{r}_i \\ \boldsymbol{r}_{jk} &= \boldsymbol{r}_k - \boldsymbol{r}_j \end{aligned} \tag{4}$$

Also, the sense of triangle rotation from small to medium to large angle is specified by the flag $I_{ccw/cw}$, where $I_{ccw/cw} = 1$ denotes counter-clockwise, $I_{ccw/cw} = -1$ denotes clockwise, and $I_{ccw/cw} = 0$ denotes an undetermined case (due to catalog parameter uncertainty).

The entire list can be represented as a matrix consisting of the lists of the individual parameters,

$$\boldsymbol{\Delta}_{list} = \left[\begin{array}{ccccccccc} \mathbf{I}_s & \mathbf{I}_m & \mathbf{I}_l & \mathbf{S} & \mathbf{L} & \boldsymbol{\Gamma}_s & \boldsymbol{\Gamma}_m & \boldsymbol{\Gamma}_l & \mathbf{I}_{ccw/cw} \end{array}\right]_{n\times 9} \tag{5}$$

where each row of the matrix consists of the entries of a single crater triangle. All of the individual parameter lists are $n \times 1$ vectors, where n is the number of crater triangles that are logged.

ERRORS IN CALCULATION/MEASUREMENT OF CRATER TRIANGLE PARAMETERS

For each crater triangle present in an image, the crater identification algorithm will measure the cosine of the smallest and largest angles of the triangle, as well as the ratios of the crater diameters to the longest leg of the triangle. The measured angle cosines and crater diameter ratios will differ from the true values due to 1) distortion in the projection of the crater triangle onto the image plane arising from attitude pointing uncertainty, and 2) measurement accuracy limitations arising from the image processing process. An attempt will be made to match the measured angle cosines and crater diameter ratios to entries in the crater triangle list (which was created from the USGS crater database[4]). The angle cosines and crater diameter ratios cataloged in the crater triangle list will be in error due the accuracy limitations of the listed values of crater latitude, longitude, and diameter provided in the USGS database. Consequently, in order to match a measured crater triangle to entries in the crater triangle list, the following error sources must be accounted for when defining search bounds: 1) USGS crater database accuracy, 2) camera pointing uncertainty and its effect on the projection of the crater triangle onto the camera image plane, and 3) accuracy of the measurements provided by the crater detection algorithm. The contribution of each error source to the difference between measured and cataloged crater triangle angle cosines and diameter ratios is discussed in this section.

Accuracy of Triangle List Parameter Calculation from Crater Catalog

The accuracy to which the triangles and diameter ratios calculated from the USGS crater database can be determined is based upon the accuracy of the parameters given in the database. Latitude and longitude of each crater location are given to within ± 0.05 degrees, while the diameter of each crater is given to within ± 0.5 km.[4] These uncertainties are assumed to be uniformly distributed.

Angle Cosine Error Analysis and Real-Time Calculation Consider the equation describing the cosine of the angle formed by two legs of a crater triangle:

$$\cos \alpha_{i_t} = \frac{\boldsymbol{r}_{ij_t}^T \boldsymbol{r}_{ik_t}}{\|\boldsymbol{r}_{ij_t}\| \|\boldsymbol{r}_{ik_t}\|} \tag{6}$$

where, for instance, $\boldsymbol{r}_{ij_t}$ is the true vector from crater i to crater j, the subscript t denotes true values of parameters, and cat denotes values cataloged in the database. Equation 6 can be expanded to 1^{st}-order about the catalog values to get an error equation describing the catalog parameter uncertainty, defined as

$$\delta(\cos \alpha)_{i_{cat}} = \cos \alpha_{i_t} - \cos \alpha_{i_{cat}} \tag{7}$$

(the derivation is omitted here for brevity[1]). However, the contribution to the overall uncertainty in the cosines of the smallest and largest angles of a measured crater triangle from the uncertainty in the cataloged latitude and longitude of the craters involved cannot be calculated directly from the aforementioned 1^{st}-order error equation in real-time. The latitude and longitude values for the detected craters are not known *a priori*, and thus the position vectors and partial derivatives of the crater locations cannot be determined. However, one can investigate the behavior of the uncertainty via monte carlo simulation. This was done for 1000 simulated craters randomly distributed around the surface of the Moon. Those that formed triangles that fit within the Apollo mapping camera field of view were used to evaluate the catalog error and the results plotted in the left-hand side of Figure 3.

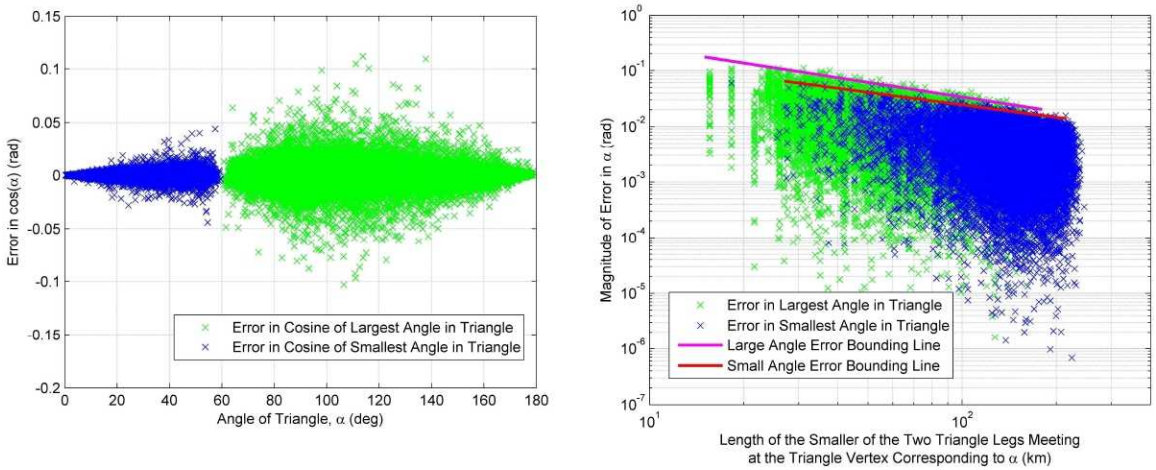

Figure 3 Error in Crater Triangle Parameters Formed From 1000 Simulated Craters Randomly Distributed Around the Surface of the Moon; Only Values for Crater Triangles that Would Fit in a $\pm 37^\circ$ Camera FOV at 124 km Altitude are Included. Left: Error in the Cosines of the Smallest and Largest Angles of Crater Triangles Plotted vs. the Smallest and Largest Angles of Each Triangle, Respectively. Right: Magnitude of the Error in the Knowledge of the Smallest and Largest Angles of Crater Triangles Plotted vs. the Length of the Shortest Leg of Each Corresponding Triangle on a Log-Log Scale.

As can be seen from Figure 3, the uncertainty in the cataloged cosine of an angle varies with the angle itself. In fact, the error in the cosine of an angle is related to the error in the angle, to 1^{st}-order, by

$$\delta(\cos\alpha) \approx -\sin(\alpha)\delta\alpha \tag{8}$$

which results from a truncated Taylor Series for $\cos(\alpha + \delta\alpha)$ expanded about α. The implication is that, if the 3σ value calculated from the $\cos(\alpha)$ errors depicted in the left-hand side of Figure 3 is used as a search bound, then for triangle angles near $\alpha = 0$ and $\alpha = \pi$, the search bound in terms of $\delta\alpha$ appears to become very large. However, when the angular error is calculated from the points in the left-hand side of Figure 3 according to

$$\delta\alpha = \alpha - \cos^{-1}\left(\cos\alpha + \delta(\cos\alpha)\right) \tag{9}$$

and graphed, the trend is very close to that seen in said figure. The angular error for very small and very large angles is actually much smaller than that for angles closer to 90 degrees. Thus, both errors ($\delta(\cos\alpha)$ and $\delta\alpha$) tend toward zero for very small and very large angles, but $\delta(\cos\alpha)$ does so much faster than $\delta\alpha$. Put another way,

$$\frac{\delta(\cos\alpha)}{\delta\alpha} = -\sin\alpha \to 0 \tag{10}$$

as $\alpha \to 0$ or $\alpha \to \pi$. In order to keep the search bounds reasonable, the statistics of $\delta\alpha$ are used to calculate search bounds, and then $\delta(\cos\alpha)$ is calculated via Equation (8), so that both terms will be bounded for all angles.

The magnitudes of the angular errors corresponding to the left-hand side of Figure 3, calculated by applying Equation (9) to each point, are graphed using a log-log scale in the right-hand side of Figure 3.

The angular errors are graphed versus the shortest of the two legs of each triangle that form the angle. Doing so yielded an obvious upper bound on the error that had the highest sensitivity. A line can be fitted to this upper bound by calculating its slope, m, and y-intercept, b. The value of the upper bound of $\delta\alpha_i$, denoted u_{α_i}, for a given value of the length of the shortest triangle leg connected to the triangle vertex at crater i, r_{min}, can then be calculated from

$$\log_{10} u_{\alpha_i} = m \log_{10} r_{min} + b \tag{11}$$

where

$$r_{min} = \min\left(\|\boldsymbol{r}_{ij}\|, \|\boldsymbol{r}_{ik}\|\right) \tag{12}$$

Solving for u_{α_i} yields

$$u_{\alpha_i} = 10^b r_{min}^m \tag{13}$$

The values of m and b corresponding to the bounding lines depicted in Figure 3 are given in Table 1.

Table 1. Bounding Line Parameters Corresponding to the Bounding Lines Depicted in Figure 3

Bounding Line Descriptor	m	b
Small Angle Error	-0.7410	-0.1302
Large Angle Error	-0.8657	0.2586

Equation (13) can be evaluated for the largest and smallest angles in a detected crater triangle by noting that the measured (in pixels) length of the shortest triangle leg, b_{min}, is related to r_{min} by

$$r_{min} \approx \frac{h}{f} b_{min} \tag{14}$$

where f is the camera focal length, measured in pixels, and h is the minimum expected altitude in low lunar orbit ($h = 100$ km for the Apollo images). The minimum altitude is used to ensure the upper bound estimate is conservative since the true altitude is not known *a priori* (according to Figure 3, the uncertainty increases with decreasing altitude).

Crater Diameter Ratio Error Analysis and Real-Time Calculation What is termed the crater diameter ratio is actually the ratio of the diameter of each crater comprising a crater triangle to the length of the longest leg of that triangle. Assume a crater triangle is made of craters i, j, and k, and that the length of the legs of the triangle are $\|\boldsymbol{r}_{ij}\|$, $\|\boldsymbol{r}_{ik}\|$, and $\|\boldsymbol{r}_{jk}\|$ (see Figure 1). The crater diameter ratio for crater i is defined as

$$\gamma_i = \frac{d_i}{r_{max}} \tag{15}$$

where r_{max} is found from

$$r_{max} = \max\left(\|\boldsymbol{r}_{ij}\|, \|\boldsymbol{r}_{ik}\|, \|\boldsymbol{r}_{jk}\|\right) \tag{16}$$

Equation 15 can be expanded about the cataloged parameter values to 1^{st}-order to get an equation describing the uncertainty in the crater diameter ratio values calculated from the catalog,

$$\delta\gamma_{i_{cat}} = \gamma_{i_t} - \gamma_{i_{cat}} \tag{17}$$

An upper bound on $3\sqrt{E\left[\left(\delta\gamma_{i_{cat}}\right)^2\right]}$, denoted u_{γ_i}, can be found in the same manner in which Equation (13) was derived:

$$u_{\gamma_i} = 10^b r_{max}^m \tag{18}$$

where the values of m and b have been found to be

$$\begin{aligned} m &= -1.6173 \\ b &= 1.4918 \end{aligned} \tag{19}$$

and

$$r_{max} \approx \frac{h}{f} b_{max} \tag{20}$$

is used to approximate r_{max}, analogous to Equation (14).

Accuracy of Triangle Projection onto Image Plane

The projection of a crater triangle onto the camera image plane is a 3D to 2D perspective projection. Differences between the projected value of a crater triangle angle cosine and the true value arise out of pointing deviations from nadir. The per-axis pointing accuracy requirement for portions of Apollo missions that made use of the mapping camera was $\pm 2^\circ$, however, the dead bands were actually specified as $\pm 0.5^\circ$.[7] Altitude is not a factor in crater triangle parameter projection accuracy to 1^{st}-order.

Angle Cosine Error Analysis and Real-Time Calculation Consider a representation of Equation 6 in terms of camera frame coordinates (and in units of pixels),

$$\cos\alpha_{i_p} = \frac{\boldsymbol{b}_{ij}^T \boldsymbol{b}_{ik}}{\|\boldsymbol{b}_{ij}\|\|\boldsymbol{b}_{ik}\|} \tag{21}$$

where the subscript p denotes the projected value (projected onto the image plane), and as an example, $\boldsymbol{b}_{ij}$ denotes the vector in camera coordinates from the projection of crater i to the projection of crater j. Equation 21 can be expanded about the truth in terms of the unknown off-nadir camera pitch and yaw pointing angles to get a 1^{st}-order equation describing the unknown projection error,

$$\delta(\cos\alpha)_{i_p} = \cos\alpha_{i_p} - \cos\alpha_{i_t} \tag{22}$$

Following the previous discussion about angle vs. angle cosine uncertainty, real-time evaluation of the uncertainty in $\cos\alpha_i$ due to the projection of the crater triangle onto the image plane is calculated by mapping the corresponding angular uncertainty statistics to cosine uncertainty statistics via Equation (8).

The error in α_i due to the projection of the crater triangle onto the image plane is a function of the uncertainty in the per-axis angular deviation of the camera pointing vector from nadir. To evaluate the nature of this error, 5000 randomly simulated crater triangles were created within the Apollo mapping camera field of view, and a random pointing error was generated for each with random per-axis pointing errors drawn from a zero mean, Gaussian distribution with a 3σ value of 2°. The perspective projection of each simulated crater triangle onto the image plane was calculated, and the error in the projected values of the smallest and largest angles determined. The resulting error value was determined to be

$$3\sqrt{E\left[\left(\delta\alpha_{i_p}\right)^2\right]} = 0.0175 \text{ rad} \tag{23}$$

which is approximately equal to the smallest value on either bounding line describing the error in α due to catalog uncertainty (see Figure 3).

Since no knowledge of instantaneous pointing uncertainty is assumed to be available during real-time image processing, the uncertainty in α due to the projection of the crater triangle onto the camera image plane is set to the constant value in Equation (23), and the uncertainty in $\delta(\cos\alpha)_{i_p}$ is then calculated from (see Equation (8))

$$3\sqrt{E\left[\left(\delta(\cos\alpha)_{i_p}\right)^2\right]} = 0.0175\sin\alpha_i \tag{24}$$

The value of $\sin\alpha_i$ is set to the measured value from the image of the crater triangle.

Crater Diameter Ratio Error Analysis and Real-Time Calculation The mapping between a crater and its projection onto the image plane is more complicated, and space does not permit its exposition here.[1] The result is that the error in the value of the projected crater radius as a function of pointing uncertainty is higher than 1^{st}-order in terms of the pointing uncertainty, and so can be neglected. Thus, the 1^{st}-order error in the calculation of a crater diameter ratio arising from its projection onto the camera image plane,

$$\delta\gamma_{i_p} = \gamma_{i_p} - \gamma_{i_t} \tag{25}$$

is only considered to be a function of the uncertainty in the projection of the length of the longest leg of the crater triangle.

The expected value of the error in the projection of the crater diameter ratio was evaluated via the monte carlo setup described earlier in this section (the crater diameter values used were drawn from a random uniform distribution with bounds 11 km $\leq d_i \leq$ 42 km). The 3σ value of the resulting error distribution was calculated to be

$$3\sqrt{E\left[\left(\delta\gamma_{i_p}\right)^2\right]} = 0.0054 \tag{26}$$

which is approximately equal to the smallest value on the bounding line describing the error in γ due to catalog uncertainty. Since no knowledge of instantaneous pointing uncertainty is assumed to be available during real-time image processing, the uncertainty in γ due to the projection of the crater triangle onto the camera image plane is set to the constant value in Equation (26).

Accuracy of Measurement of Triangle Projection on Image Plane

The accuracy with which the locations and diameters of the craters in the image plane can be measured will partially determine the accuracy with which the crater triangle angle cosines and diameter ratios can be calculated. The crater position and diameter measurements are provided by a crater detection filter. The error in these measurements is difficult to determine due to the fact that craters are not smooth ellipses, but rather, have rough and sometimes irregularly shaped rims. Experience leads us to assume the crater location and radius errors are independent, zero mean, Gaussian random variables with variances defined for a crater i of radius r_i by

$$\begin{aligned} E[\delta x_i^2] = E[\delta y_i^2] &= \left(\frac{1}{3}\max\left(\left(\text{round}\left(\frac{r_i}{10}\right) - 1\right), 1\right)\right)^2 \\ E[\delta r_i^2] &= \left(\frac{1}{3}\text{round}\left(\frac{r_i}{10}\right)\right)^2 \end{aligned} \tag{27}$$

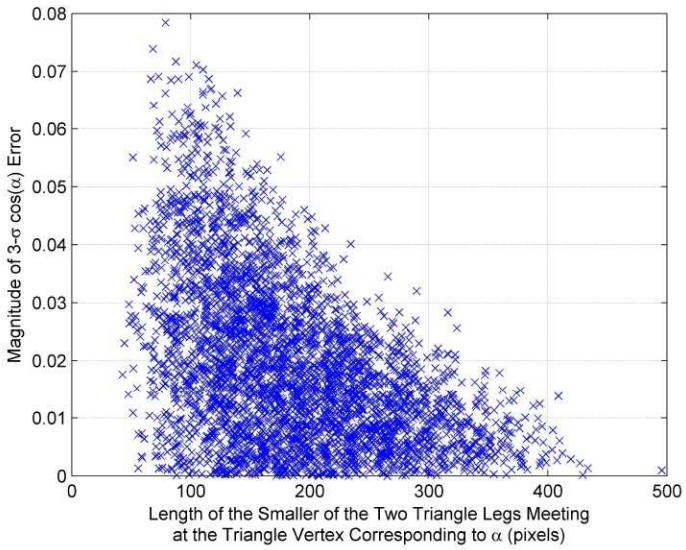

Figure 4 Uncertainty (3σ) in the Measured Angle Cosines of 5000 Randomly Simulated Crater Triangles as Projected onto the Camera Image Plane, Plotted vs. the Length of the Shorter of the Two Triangle Legs Forming the Angle in Question

The terms δx_i and δy_i in Equation (27) represent the errors in x_{c_i} and y_{c_i}, the crater coordinates in the image plane. The term δr_i represents the error in the measured radius of crater i. All parameters are specified in units of pixels.

Angle Cosine Error Analysis and Real-Time Calculation The difference between the measured angle cosine and the value of its projection on the image plane can be analyzed by expanding Equation 21 about the measured values to 1^{st}-order in terms of the uncertainty in the coordinates of the crater locations. The fact that all of the variables in the derived equation are measured quantities allows for the development of an equation describing the variance of the measurement error which can be evaluated on a per-triangle basis in real-time.

Figure 4 illustrates the benefit of a geometry-dependent approach, rather than the error bounding line approach employed to find the uncertainty in $\cos\alpha_i$ due to crater catalog uncertainties (see Figure 3). For each of 5000 simulated crater triangles formed from craters randomly distributed in the camera image plane (from a uniform distribution), the estimate of the measurement error uncertainty was calculated and plotted. Only those values corresponding to crater triangles composed of non-overlapping craters were considered. Crater radii were randomly distributed between the values of 14 pixels and 66 pixels assuming a uniform distribution (the dimensions of the camera field of view were assumed to be 450×450 pixels).

As seen in Figure 4, in most cases the computed uncertainty in the measurement of $\cos\alpha_{i_p}$ is much less than would be indicated by an error bounding line, which would be an upper bound on all errors. The smaller uncertainty value allows for a more efficient crater triangle list search.

Crater Diameter Ratio Error Analysis and Real-Time Calculation Expansion of the crater diameter ratio equation about its measured value in terms of the measurement uncertainties given in Equation 27 leads to a 1^{st}-order equation describing the uncertainty in the measurement of the

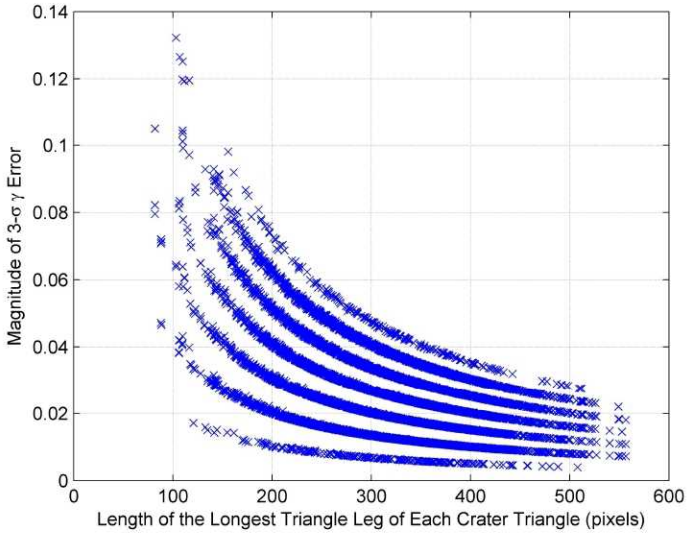

Figure 5 Uncertainty (3σ) in the Measured Crater Diameter Ratios of 5000 Randomly Simulated Crater Triangles as Projected onto the Camera Image Plane, Plotted vs. the Length of the Shorter of the Two Triangle Legs Forming the Angle in Question

diameter ratio due to its projection onto the image plane. This value can also be calculated in real-time based on measurements from each individual crater triangle, which allows for a reduction of the crater triangle search space. The monte carlo simulation that was used to generate Figure 4 was also used to generate Figure 5, which shows the crater diameter ratio measurement uncertainty.

As an aside, note the discrete steps between curves in Figure 5. The phenomenon results from the discrete nature of Equation (27).

Real-Time Calculation of Crater Triangle Search Bounds

The task of the crater identification algorithm is to match measured crater triangle parameters to those cataloged in the crater triangle list created from the USGS crater database.[4] This involves a search of the crater triangle list which in turn requires numeric search bounds.

The search bounds on $\cos\alpha_i$ are calculated from ± 2 times the root sum square (RSS) of the 1-σ contribution of each error source to the uncertainty between the measured and cataloged values of the crater triangle angle cosines:

$$\Delta(\cos\alpha)_i = 2\sqrt{E\left[(\delta(\cos\alpha)_{i_m})^2\right] + E\left[(\delta(\cos\alpha)_{i_p})^2\right] + \left(\frac{u_{\alpha_i}\sin\alpha_i}{3}\right)^2} \tag{28}$$

where $E\left[(\delta(\cos\alpha)_{i_m})^2\right]$ is the measurement uncertainty calculated directly from an error equation, $E\left[(\delta(\cos\alpha)_{i_p})^2\right]$ is calculated from Equation (24), u_{α_i} is a upper bound calculated from Equation (13), and $\sin\alpha_i$ is the measured sine of the angle under consideration (see Equation (8) for an explanation). Twice the standard deviation is used for the search bounds because 95% of the crater triangles that match the measured one to within tolerances will still be found, but the search

space will be reduced by $1/3$, which will reduce the number of false identifications. Equation (28) is evaluated for the smallest and largest angle in each crater triangle to get the search bounds for each.

Similarly, the search bounds on γ_i are calculated from ± 2 times the RSS of the 1-σ contribution of each error source to the uncertainty between the measured and cataloged values of the crater diameter ratios:

$$\Delta\gamma_i = 2\sqrt{E\left[\left(\delta\gamma_{i_m}\right)^2\right] + E\left[\left(\delta\gamma_{i_p}\right)^2\right] + \left(\frac{u_{\gamma_i}}{3}\right)^2} \tag{29}$$

where $E\left[\left(\delta\gamma_{i_m}\right)^2\right]$ is the measurement uncertainty calculated directly from an error equation, $E\left[\left(\delta\gamma_{i_p}\right)^2\right]$ is calculated from Equation (26), and u_{γ_i} is a upper bound on 3σ values calculated from Equation (18). Equation (29) is evaluated for all 3 crater diameter ratios formed from a given crater triangle to get the search bounds for each.

CRATER TRIANGLE SEARCH TECHNIQUE

The previously described crater pattern matching strategy employs two reference craters as a base with which to form triangles with the remaining detected craters. These triangles can be compared against a list of known crater triangles pre-computed from the USGS crater database,[4] denoted $\mathbf{\Delta}_{list}$ in Equation (5). If the reference crater pair does not produce an acceptable match, a new reference crater pair is chosen and the process repeated. Failure to produce an acceptable match could be due to bad geometry, or to the fact that one or both of the reference craters are not actually in the USGS database (a common occurrence). In fact, all possible reference crater pairs detected in the image are checked to locate the one that produces the best match in terms of probability.

Thus, for each triangle that can be formed from two reference craters and another of the detected craters within an image, a list must be compiled of all of the crater triangles in $\mathbf{\Delta}_{list}$ that match the observed crater triangle to within measurement tolerances. This list will be denoted as a matching triangle list. Since the search process is repeated for all possible pairs of reference craters, such lists must be created for every triangle that can by formed by every combination of reference crater pairs. Say, for instance, that n craters are detected in an image by the crater detection algorithm. For a given reference crater pair in this scenario, $n-2$ individual matching triangle lists must be created. In order to repeat the process for every combination of reference craters, the number of matching triangle list evaluations would be

$$\left(\frac{n(n-1)}{2}\right)(n-2) \tag{30}$$

For a value of $n = 9$, the result is that 252 matching triangle lists must be created. A gain in computational efficiency can be realized by noting that there are only

$$\frac{n(n-1)(n-2)}{3 \cdot 2} \tag{31}$$

unique crater triangles in the image (for $n = 9$, the number is 84). Thus, the first thing that is done during the crater triangle search portion of the algorithm is that each unique detected crater triangle in the image is evaluated to create its matching triangle list and the lists recorded for future retrieval.

Once all of the matching triangle lists have been created, the possible reference crater combinations are cycled through. For each reference pair, the relevant matching triangle lists are concatenated so as to form a list of possible candidates for the first reference crater, and a corresponding

list of possible candidates for the second reference crater. This reference crater list is searched for the mode (in terms of crater pairs), and if unique, the match is checked for the probability that it is a false match. This part of the crater search technique was adapted from the star pattern search techniques presented in[8] and.[9] The reference crater pair match with the lowest probability of being a false match is kept, provided the probability is lower than a threshold. A high level flowchart of the crater identification algorithm is depicted in Figure 6.

Matching Triangle List Creation

The efficiency of the search of $\mathbf{\Delta}_{list}$ for entries that match an observed crater triangle to within measurement tolerances can be greatly enhanced through use of the k-vector search technique.[10] The pre-computed crater triangle list, $\mathbf{\Delta}_{list}$, was arranged such that the known triangles are listed in order of increasing values of $\cos\alpha_s$. That is, $\mathbf{\Delta}_{list}$ was arranged such that the entries in the $n \times 1$ vector $\mathbf{S}$ were in ascending order. This was done so that the search space could be quickly reduced (via the k-vector technique) by finding the range of triangles that satisfy

$$(\cos\alpha_s)_{min} \leq \cos\alpha_s \leq (\cos\alpha_s)_{max} \tag{32}$$

without conducting an actual element-by-element search. To enable a brief explanation of the k-vector search technique, let a straight line,

$$z(x) = mx + q \tag{33}$$

connect the points just below the minimum value of $\cos\alpha_s$ and just above the maximum value of $\cos\alpha_s$, such that

$$\begin{aligned} m &= \frac{\mathbf{S}(n) - \mathbf{S}(1) + 2\xi}{n-1} \\ q &= \mathbf{S}(1) - m - \xi \end{aligned} \tag{34}$$

where ξ is a tolerance value. The i^{th} element in the k-vector is determined according to the rule $k(i) = j$, where

$$\mathbf{S}(j) \leq z(i) < \mathbf{S}(j+1) \tag{35}$$

(The i^{th} entry in the k-vector is essentially the number of entries in $\mathbf{S}$ that are less than the value $z(i)$.) To find the indices of entries in $\mathbf{S}$ falling between the values $(\cos\alpha_s)_{min}$ and $(\cos\alpha_s)_{max}$, all that is needed is to calculate i_{min} and i_{max} such that

$$\begin{aligned} i_{min} &= \left\lfloor \frac{(\cos\alpha_s)_{min} - q}{m} \right\rfloor \\ i_{max} &= \left\lceil \frac{(\cos\alpha_s)_{max} - q}{m} \right\rceil \end{aligned} \tag{36}$$

from which the relevant $\mathbf{S}$ indices are found according to

$$\begin{aligned} j_{start} &= k(i_{min}) + 1 \\ j_{end} &= k(i_{max}) \end{aligned} \tag{37}$$

For more information on the k-vector search technique, see[8] and.[10]

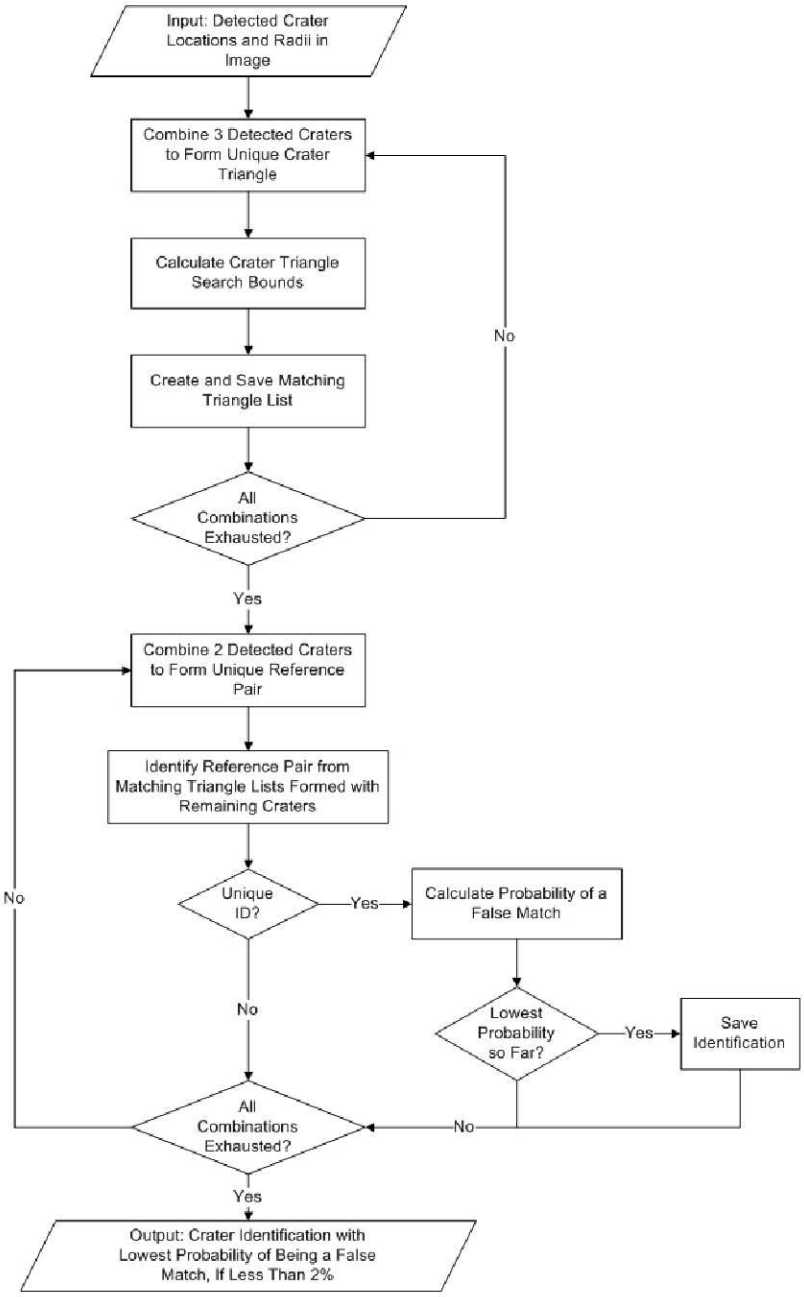

Figure 6. High Level Flowchart of Crater Identification Algorithm

A matching triangle list for a given detected crater triangle, Δ_{ijk} (note that notation is abused here with multiple definitions of i, j, and k, but the meaning of each should be clear from the context), is found by first calculating the cosine of the smallest measured angle of the triangle. Then, the search bounds on $\cos\alpha_s$ are calculated via an appropriately referenced version of Equation (28), so that

$$\begin{aligned}(\cos\alpha_s)_{min} &= \cos\alpha_s - \Delta(\cos\alpha_s) \\ (\cos\alpha_s)_{max} &= \cos\alpha_s + \Delta(\cos\alpha_s)\end{aligned} \tag{38}$$

At this point, the k-vector technique can be applied to reduce the search space from the almost 500000 possible pre-computed crater triangles in $\mathbf{\Delta}_{list}$, to a much smaller number that match the cosine of the smallest angle of the measured triangle to within measurement tolerances. This subset of the search space is then searched for triangles that match the cosine of the largest angle of the measured triangle to within the measurement tolerances. The required parameters are calculated via an appropriately referenced version of Equation (28) to get the search bounds

$$\begin{aligned}(\cos\alpha_l)_{min} &= \cos\alpha_l - \Delta(\cos\alpha_l) \\ (\cos\alpha_l)_{max} &= \cos\alpha_l + \Delta(\cos\alpha_l)\end{aligned} \tag{39}$$

Each triangle in the search subspace generated from the k-vector technique is examined individually in this step for compliance with the condition

$$(\cos\alpha_l)_{min} \leq \cos\alpha_l \leq (\cos\alpha_l)_{max} \tag{40}$$

and a new search subspace is formed. The search subspace reduction process is continued via individual application of the following criteria:

$$\begin{aligned}&(\gamma_s)_{min} \leq \gamma_s \leq (\gamma_s)_{max} \\ &(\gamma_m)_{min} \leq \gamma_m \leq (\gamma_m)_{max} \\ &(\gamma_l)_{min} \leq \gamma_l \leq (\gamma_l)_{max} \\ &I_{ccw/cw}\left(I_{ccw/cw}\right)_{meas} \geq 0\end{aligned} \tag{41}$$

The crater diameter ratio search bounds are computed from appropriately referenced versions of Equation (29), where the subscripts s, m, and l denote the craters corresponding to the vertices associated with the smallest, middle, and largest angles of the crater triangle, respectively. The measured sense of $s \rightarrow m \rightarrow l$ triangle rotation, as viewed from above, is set to zero (assumed indeterminate) if it cannot be definitively measured, as determined by the failure of any one of the following three checks:

$$\begin{aligned}\cos\alpha_s - \cos\alpha_m - 3\sqrt{E\left[\left(\delta(\cos\alpha_s)_m\right)^2\right]} &< 0 \\ \cos\alpha_m - \cos\alpha_l - 3\sqrt{E\left[\left(\delta(\cos\alpha_l)_m\right)^2\right]} &< 0 \\ \cos\alpha_s + 3\sqrt{E\left[\left(\delta(\cos\alpha_s)_m\right)^2\right]} &> 1\end{aligned} \tag{42}$$

where $E\left[\left(\delta(\cos\alpha_s)_m\right)^2\right]$ and $E\left[\left(\delta(\cos\alpha_l)_m\right)^2\right]$ are measurement uncertainties calculated from geometry-dependent error equations. (The checks in Equations (42) are used to verify that the

difference between two angles is larger than the uncertainty in the value of that difference in order to properly rank the angles; however, the uncertainty and correlations due to the measurement of the cosine of the middle angle are ignored for algorithm efficiency.) Otherwise, sense of triangle rotation is calculated based on the sign of

$$(\hat{\boldsymbol{u}}_f \times \boldsymbol{b}_{sm}) \cdot \boldsymbol{b}_{sl} \tag{43}$$

where $\hat{\boldsymbol{u}}_f = \begin{bmatrix} 0 & 0 & 1 \end{bmatrix}$, $\boldsymbol{b}_{sm} = \boldsymbol{b}_m - \boldsymbol{b}_s$ is the measured vector (in pixels) from the vertex of the smallest angle of the triangle to the vertex of the middle angle of the triangle, and $\boldsymbol{b}_{sl} = \boldsymbol{b}_l - \boldsymbol{b}_s$ is the measured vector (in pixels) from the vertex of the smallest angle of the triangle to the vertex of the largest angle of the triangle. If the quantity has a positive sign, the sense of rotation is counter-clockwise. A negative sign corresponds to a clockwise sense of rotation from small to medium to large angles. In mathematical terms

$$\left(I_{ccw/cw}\right)_{meas} = \begin{cases} 0, & \begin{cases} \cos\alpha_s - \cos\alpha_m - 3\sqrt{E\left[\left(\delta(\cos\alpha_s)_m\right)^2\right]} < 0 \quad \text{or} \\ \cos\alpha_m - \cos\alpha_l - 3\sqrt{E\left[\left(\delta(\cos\alpha_l)_m\right)^2\right]} < 0 \quad \text{or} \\ \cos\alpha_s + 3\sqrt{E\left[\left(\delta(\cos\alpha_s)_m\right)^2\right]} > 1 \end{cases} \\ 1, & (\hat{\boldsymbol{u}}_f \times \boldsymbol{b}_{sm}) \cdot \boldsymbol{b}_{sl} > 0 \\ -1, & (\hat{\boldsymbol{u}}_f \times \boldsymbol{b}_{sm}) \cdot \boldsymbol{b}_{sl} < 0 \end{cases} \tag{44}$$

The result of this process is the list of known crater triangles that meet the criteria in Equations (32), (40), and (41) for the measured crater triangle Δ_{ijk}. This list is given in terms of crater identification number triples. As noted in Equation (5), each entry in the pre-computed crater triangle list contains the identification numbers of the craters which form the triangle, listed in order from that at the vertex of the smallest angle in the triangle to the largest. Using this same paradigm, if $\boldsymbol{v}_r$ denotes the indices of the rows in $\boldsymbol{\Delta}_{list}$ that match the observed triangle, then the matching triangle list for Δ_{ijk} is given by

$$\boldsymbol{\Delta}_r = \begin{bmatrix} \mathbf{I}_s(\boldsymbol{v}_r) & \mathbf{I}_m(\boldsymbol{v}_r) & \mathbf{I}_l(\boldsymbol{v}_r) \end{bmatrix} \tag{45}$$

where r is the scalar index used to store each matching triangle list for later retrieval. The scalar index is calculated, assuming the crater indices are such that $i < j < k$, according to

$$r = \left(\sum_{i_2=1}^{i-1} \frac{(n-i_2)(n-i_2-1)}{2}\right) + \left(\sum_{j_2=i}^{j-2} (n-(j_2+1))\right) + (k-j) \tag{46}$$

In some instances, the matching triangle list for a given observed crater triangle can contain ambiguous entries. That is, a pair of craters in the database could combine with multiple other craters in the database to form triangles that match the observed triangle to within measurement precision. Such scenarios result from poor geometry for crater pattern matching, and so these "double" entries are removed from a matching crater list.

Reference Crater Pair Identification

Once the matching triangle lists have been compiled for each unique crater triangle within an image, all possible unique reference crater pairs are evaluated to determine if they can be matched to entries in the USGS crater database. To understand how this is done, assume that n craters are detected within an image, and that craters i and j are currently under consideration as reference craters, where $i \neq j$ and $i, j \leq n$. There are $n-2$ remaining craters in the image with which to form triangles with the reference craters. Consider the triangle formed by the reference craters and one of these remaining craters, k_1. Assume that in this triangle, crater k_1 is located at the vertex of the smallest angle in the triangle, crater i at the vertex of the middle angle, and crater j at the vertex of the largest angle. Further assume that the crater indices are such that $i < j < k_1$. Then, the scaler index for the required matching triangle list, r_1, is given by Equation (46) with k_1 substituted for k. The lists of candidate crater names for reference craters i and j, based on the triangle formed with crater k_1, are given by

$$\begin{aligned} \mathbf{I}_1 &= \boldsymbol{\Delta}_{r_1} \hat{\boldsymbol{u}}_m \\ \mathbf{J}_1 &= \boldsymbol{\Delta}_{r_1} \hat{\boldsymbol{u}}_l \end{aligned} \tag{47}$$

where $\boldsymbol{\Delta}_{r_1}$ is specified in Equation (45), and the column selection vectors are given by

$$\begin{aligned} \hat{\boldsymbol{u}}_s &= \begin{bmatrix} 1 & 0 & 0 \end{bmatrix}^T \\ \hat{\boldsymbol{u}}_m &= \begin{bmatrix} 0 & 1 & 0 \end{bmatrix}^T \\ \hat{\boldsymbol{u}}_l &= \begin{bmatrix} 0 & 0 & 1 \end{bmatrix}^T \end{aligned} \tag{48}$$

The column selection vectors used in Equation (47) to map the matching crater list to the observed crater triangle, Δ_{ijk_1}, were chosen based on the fact that reference crater i is located at the vertex of the middle angle of the triangle and reference crater j at the largest, and so the names in the matching crater list must be mapped accordingly. Also, the list of candidate crater names for crater k_1 is found to be

$$\mathbf{K}_1 = \boldsymbol{\Delta}_{r_1} \hat{\boldsymbol{u}}_s \tag{49}$$

Let the remaining $n-3$ craters be denoted $k_2, \ldots, k_{n-2}$. The lists of candidate crater names for reference craters i and j, based on the triangles formed with these craters, are concatenated to $\mathbf{I}_1$ and $\mathbf{J}_1$ to get

$$\begin{aligned} \mathbf{I} &= \begin{bmatrix} \mathbf{I}_1^T & \mathbf{I}_2^T & \cdots & \mathbf{I}_{n-2}^T \end{bmatrix}^T \\ \mathbf{J} &= \begin{bmatrix} \mathbf{J}_1^T & \mathbf{J}_2^T & \cdots & \mathbf{J}_{n-2}^T \end{bmatrix}^T \end{aligned} \tag{50}$$

which are used to create the two column array

$$\mathbf{IJ}_{list} = \begin{bmatrix} \mathbf{I} & \mathbf{J} \end{bmatrix} \tag{51}$$

If the mode of $\mathbf{IJ}_{list}$, in terms of its rows, is unique and occurs at least twice, it is considered a potential match for the names of the reference craters i and j. (To clarify, the row-based mode is the pair of identification numbers for craters i and j that occurs most often in the array $\mathbf{IJ}_{list}$.) Define

$\boldsymbol{v}_{ij}$ as the vector containing the indices of the rows in $\mathbf{IJ}_{list}$ corresponding to the mode. Then, with $\mathbf{K}$ specified as

$$\mathbf{K} = \left[\begin{array}{cccc} \mathbf{K}_1^T & \mathbf{K}_2^T & \cdots & \mathbf{K}_{n-2}^T \end{array} \right]^T \tag{52}$$

the names of the other craters in the image that have potentially been identified by reference craters i and j are found from $\mathbf{K}(\boldsymbol{v}_{ij})$. If any of the entries in $\mathbf{K}(\boldsymbol{v}_{ij})$ are not unique, the potential match is rejected as occurring due to bad geometry (the same crater cannot be at two different locations within the image). Otherwise, the number of craters that have been potentially identified by this match is given by 2 plus the number of entries in $\boldsymbol{v}_{ij}$.

The probability that the match corresponding to the mode of $\mathbf{IJ}_{list}$ is a false identification is calculated by the process outlined in the next section. After evaluating all of the unique reference crater pairs for potential matches from the USGS catalog in this manner, the one with the lowest probability of being a false identification is output, provided the probability is less than 2%.

PROBABILITY OF A FALSE MATCH

Every unique crater pattern identification found in the search phase is evaluated in terms of the probability that it is a false match to the craters actually observed. The USGS lunar crater database is not a complete list of the craters on the Moon. Many of the craters found in an image by the crater detection algorithm are not in the database. To avoid incorrectly identifying these uncataloged craters (or any of the less frequent spurious responses from the crater detection algorithm), any identification of a set of craters in an image with an unacceptably high probability of being a false identification is discarded.

Probability Equation Derivation

Consider the probability of false identification of the crater triangle depicted in Figure 1. Let I denote the event that crater i is in the USGS lunar crater database. Define the events J and K for craters j and k similarly, and assume that each event (I,J,K) is mutually independent and has probability p. Denote the event that all three craters are in the crater database by

$$X = I \cap J \cap K \tag{53}$$

which has probability

$$P[X] = p^3 \tag{54}$$

Also, let A_1 denote the event that the cosine of the smallest angle of a random crater triangle is equal to that formed by detected craters i, j, and k (see Figure 1) to within the search bounds:

$$A_1 \Leftrightarrow (\cos\alpha_s)_{min} \leq \cos\alpha_s \leq (\cos\alpha_s)_{max} \tag{55}$$

Similarly, define the events

$$\begin{aligned} B_1 &\Leftrightarrow (\cos\alpha_l)_{min} \leq \cos\alpha_l \leq (\cos\alpha_l)_{max} \\ C_1 &\Leftrightarrow (\gamma_s)_{min} \leq \gamma_s \leq (\gamma_s)_{max} \\ D_1 &\Leftrightarrow (\gamma_m)_{min} \leq \gamma_m \leq (\gamma_m)_{max} \\ E_1 &\Leftrightarrow (\gamma_l)_{min} \leq \gamma_l \leq (\gamma_l)_{max} \\ H_1 &\Leftrightarrow I_{ccw/cw} \left(I_{ccw/cw}\right)_{meas} \geq 0 \end{aligned} \tag{56}$$

If the event F_1 is defined as

$$F_1 = A_1 \cap B_1 \cap C_1 \cap D_1 \cap E_1 \cap H_1 \tag{57}$$

then the probability of interest is $P[\bar{X}|F_1]$, i.e., the probability that a crater triangle matches all of the given search criteria but contains at least one detected crater that is not in the database.

The probability $P[\bar{X}|F_1]$ can be rewritten in a more usable form via Bayes' Theorem,[11]

$$\begin{aligned} P[\bar{X}|F_1] &= \frac{P[F_1 \cap \bar{X}]}{P[F_1]} \\ &= \frac{P[F_1|\bar{X}]P[\bar{X}]}{P[F_1|\bar{X}]P[\bar{X}] + P[F_1|X]P[X]} \end{aligned} \tag{58}$$

Since X and $\bar{X}$ partition the probability space, $P[\bar{X}] = 1 - p^3$. Furthermore, $P[F_1|X]$ can be found from

$$P[F_1|X] = \frac{M_1}{N_3} \tag{59}$$

where N_3 is the total number of crater triangles in the search list, and M_1 is the number of those triangles that satisfy all the search criteria specified by event F_1, so that

$$P[\bar{X}|F_1] = \frac{P[F_1|\bar{X}](1-p^3)}{P[F_1|\bar{X}](1-p^3) + \frac{M_1}{N_3}p^3} \tag{60}$$

This can be extended to include a second crater triangle. Consider a second crater triangle, Δ_{ijm}, as seen in Figure 2, that shares two craters (the reference craters) with the first crater triangle. Define events A_2, B_2, C_2, D_2, E_2, H_2, and F_2 for the second crater triangle in a manner analogous to Equations (55), (56), and (57). Then let the event X be redefined as

$$X = I \cap J \cap K \cap M \tag{61}$$

where M is the event that crater m is in the USGS lunar crater database. The probability of interest is now $P[\bar{X}|(F_1 \cap F_2)]$, i.e., the probability that both crater triangles match all of the given search criteria but contain at least one detected crater that is not in the database. Using Bayes' theorem, this probability can be rewritten as

$$P[\bar{X}|(F_1 \cap F_2)] = \frac{P[(F_1 \cap F_2)|\bar{X}]P[\bar{X}]}{P[(F_1 \cap F_2)|\bar{X}]P[\bar{X}] + P[(F_1 \cap F_2)|X]P[X]} \tag{62}$$

To simplify Equation (62), the conservative assumption is made that craters i and j form the longest leg of both triangles, which yields the result $C_2 \cap D_2 = C_1 \cap D_1$. Therefore, define the event

$$G_2 = A_2 \cap B_2 \cap E_2 \cap H_2 \tag{63}$$

Under the additional assumption that the events F_1 and G_2 are conditionally independent (given $\bar{X}$), $P[(F_1 \cap F_2)|\bar{X}]$ can be rewritten as

$$P[(F_1 \cap F_2)|\bar{X}] \approx P[(F_1 \cap G_2)|\bar{X}] = P[F_1|\bar{X}]P[G_2|\bar{X}] \tag{64}$$

Substitution of Equation (64) into Equation (62), and using $P[X] = p^4$, yields

$$P[\bar{X}|(F_1 \cap F_2)] \approx \frac{P[F_1|\bar{X}]P[G_2|\bar{X}](1-p^4)}{P[F_1|\bar{X}]P[G_2|\bar{X}](1-p^4) + \frac{M_2}{N_4}p^4} \tag{65}$$

where N_4 is the total number of admissible (within the camera FOV) crater quadrilaterals that can be constructed from the crater triangle search list, and M_2 is the number of those triangle pairs that satisfy all the search criteria specified by events F_1 and F_2, and have the same pair of reference craters.

Equation (65) can be expanded to apply to the case of n crater triangles formed from the two reference craters and n additional craters. Assume only one pair of reference craters in the crater database satisfies all search criteria, $F_1 \cap \cdots \cap F_n$, and the number of $(n+2)$-sided crater polygons that can be constructed from the USGS lunar crater database, and viewed within the camera FOV, is specified as N_{n+2}. Then, the probability that all n crater triangles match all of the given search criteria, but contain at least one detected crater that is not in the database, is approximated by

$$P[\bar{X}|(F_1 \cap \cdots \cap F_n)] \approx \frac{P[F_1|\bar{X}]\left(\prod_{i=2}^{n} P[G_i|\bar{X}]\right)(1-p^{n+2})}{P[F_1|\bar{X}]\left(\prod_{i=2}^{n} P[G_i|\bar{X}]\right)(1-p^{n+2}) + \frac{1}{N_{n+2}}p^{n+2}} \tag{66}$$

Probability Equation Real-Time Evaluation

The two quantities that must be determined to evaluate Equation (66) in real-time are the value of N_{n+2} and value of the product $P[F_1|\bar{X}]\left(\prod_{i=2}^{n} P[G_i|\bar{X}]\right)$. The parameter N_{n+2} represents the total number of $(n+2)$-sided crater polygons that can be constructed from the USGS crater database by craters that could potentially be in the camera FOV simultaneously.

Consider a pair of craters that have the potential to be within the camera FOV simultaneously, and k additional craters such that all $k+2$ craters have the potential to be within the camera FOV simultaneously. The number of $(n+2)$-sided crater polygons that can be formed from the reference pair and the k additional craters is given by

$$\frac{k!}{(k-n)!n!} \tag{67}$$

which arises from the fact that the k additional craters are taken n at a time with no repetitions, and combinations are sought, rather than permutations. Using this result, and the assumption that all admissible (within the FOV) crater triangles formed from a reference pair of craters and k additional craters are simultaneously admissible, the values of N_{n+2} for $n = 1, \ldots, 12$ were calculated. Note that the aforementioned assumption is conservative, in that it will tend to overestimate N_{n+2}, which will in turn cause $P[\bar{X}|(F_1 \cap \cdots \cap F_n)]$ to be overestimated from Equation (66), making the algorithm more discriminative.

The task of calculating the product $P[F_1|\bar{X}]\left(\prod_{i=2}^{n} P[G_i|\bar{X}]\right)$ in real-time is made easier by assuming that the probability distribution describing the locations and diameters of non-cataloged craters is approximately equal to that of the cataloged craters. Thus, the value $P[F_1|\bar{X}]$ can be approximated by

$$P[F_1|\bar{X}] \approx \frac{M_1}{N_3} \tag{68}$$

where M_1 is the number of cataloged crater triangles that satisfy the search criteria specified by event F_1, as applied to the first triangle evaluated for a given pair of reference craters. Similarly, the values of $P[G_i|\bar{X}]$ can be approximated by

$$P[G_i|\bar{X}] \approx \frac{R_i}{N_3} \tag{69}$$

where R_i is the number of cataloged crater triangles that satisfy the search criteria specified by event G_i, as applied to the i^{th} $(i > 1)$ triangle evaluated for a given pair of reference craters.

Substitution of Equations (68) and (69) into Equation (66) yields the real-time approximation used to determine the probability that a particular uniquely-identified crater pattern is a false match:

$$P[\bar{X}|(F_1 \cap \cdots \cap F_n)] \approx \frac{\frac{M_1}{N_3}\left(\prod_{i=2}^{n}\frac{R_i}{N_3}\right)(1-p^{n+2})}{\frac{M_1}{N_3}\left(\prod_{i=2}^{n}\frac{R_i}{N_3}\right)(1-p^{n+2}) + \frac{1}{N_{n+2}}p^{n+2}} \tag{70}$$

A value of $p = 0.5$ was adopted for real-time evaluation of Equation (70) based on experience. If an identified crater pattern is estimated to have a greater than 2% probability of being a false match, it is rejected. A more accurate and/or more complete crater database would allow for a reduction of this threshold.

RESULTS

The crater detection and identification algorithms were tested on images from the Apollo mapping camera taken during the Apollo 16 mission, which were obtained courtesy of the Lunar Planetary Institute.[6] The mapping camera had a 37 degree half angle field of view (FOV), and used film.[7] The images have since been scanned, digitized, and re-sized for this investigation to approximately 450×450 pixels (maintaining the aspect ratio) to ease the computational burden of processing. The film was 4.5 inches square and the lens focal length was 3 inches which translates to 300 pixels in length for the re-sampled images.

The image collection contained images from 17 orbits of Apollo 16 and the departure from the Moon. The first two orbits, revolutions 3 and 4, contained very few images, and so were discarded. The images from revolutions 25, 26, 27, 37, 48, and 59 were taken at either 25 degree or 40 degree camera tilt angles from nadir, and so were unusable for crater detection and identification (a nadir pointing camera is required). Of the remaining 9 revolutions of data, the majority of the images in 5 revolutions were obscured by what appeared to be an antenna. These revolutions (numbers 29, 38, 39, 47, and 60) were discarded. Thus, 4 revolutions of images remained with which to test the crater identification algorithm. These were revolutions 17, 18, 28, and 63.

Images from the 4 usable revolutions of images were processed by a crater detection algorithm,[1] which attempted to find up to 15 craters in the image within a certain size range. The locations and diameters of the detected craters were then fed to the crater identification routine which attempted to match them to known craters in the USGS database. A solar elevation angle mask of less than 5 degrees and greater than 50 degrees was applied to each dataset so that only images with good lighting were processed. Also, the presence or absence of cataloged craters within an image was determined by visual inspection using the unnamed crater imaging tool from the USGS Gazetteer of Planetary Nomenclature website.[4]

Apollo 16 Mapping Camera Image Analysis

Some sample results from revolution 17 are presented in Figure 7, with the detected and identified craters denoted on each image. Both falsely identified and correctly identified craters are named in the images. Of the images in Figure 7, only AS16-M-0040 depicts an incorrect identification.

For instance, the image AS16-M-0037 in Figure 7 contains 7 cataloged craters, all of which were detected by the crater detection algorithm, as well as 3 other non-cataloged craters. The crater identification algorithm correctly identified 6 of the detected craters as Dufay B, Dufay D, Dufay X, Dufay Y, Spencer Jones J, and Spencer Jones K, and estimated that the probability of the result being a false ID was on the order of $6.8 \times 10^{-6}\%$. Since the probability was less than the 2% threshold, the identification was accepted as correct by the algorithm.

An example of a false identification that was rejected by the algorithm is given in image AS16-M-0040 of Figure 7. This image contains only 1 cataloged crater that was detected by the crater detection filter, however, four of the craters in the image were identified as Manzinus U, Mutus E, Mutus X, and Nearch C. The calculated probability of a false ID was on the order of 14%, and thus the identification was rejected by the algorithm.

Note also the image AS16-M-0038 in Figure 7. In this image, 9 craters were detected by the crater detection algorithm, but only 4 of them are actually cataloged craters. This is a common occurrence on the far side of the Moon. The crater identification algorithm was able to correctly identify the 4 cataloged craters amongst the "noise" of the 5 uncataloged craters, and the identification passed the probability test. Indeed, on revolution 18 approximately the same image occurred, except 6 uncataloged craters were detected by the crater detection algorithm. The result was the same, however, with a correct identification of the 4 cataloged craters.

The performance of the crater identification algorithm is summarized in Table 2. The crater identification success rate was found to be 65% when considering images that were correctly identified, and 46% when restricting the criteria to those correctly identified and accepted by the probability test. When looking only at images in which 5 or more cataloged craters were detected (see Table 3), these numbers jump to 89% and 82%, respectively. (These numbers would be better if not for the apparently erroneous catalog value for the diameter of the crater Mills, which causes 2 of the incorrect identifications noted in Table 3.) It appears that having 5 detected craters in an image is an important discriminator as far as correct crater identification is concerned. Perhaps most impressively, every one of the 66 incorrectly identified images was rejected by the probability test.

The occurrence of so many incorrect identifications arises from the significant number of uncataloged craters on the far side of the Moon, and the relatively large uncertainties in the recorded values of latitude, longitude, and crater diameter of those craters that are cataloged. Many images with 4 detected cataloged craters result in multiple crater identifications that match the detected craters to within search tolerances. Reducing the uncertainty in the cataloged crater parameters would allow for a search tolerance reduction, thereby resulting in more unique correct identifications.

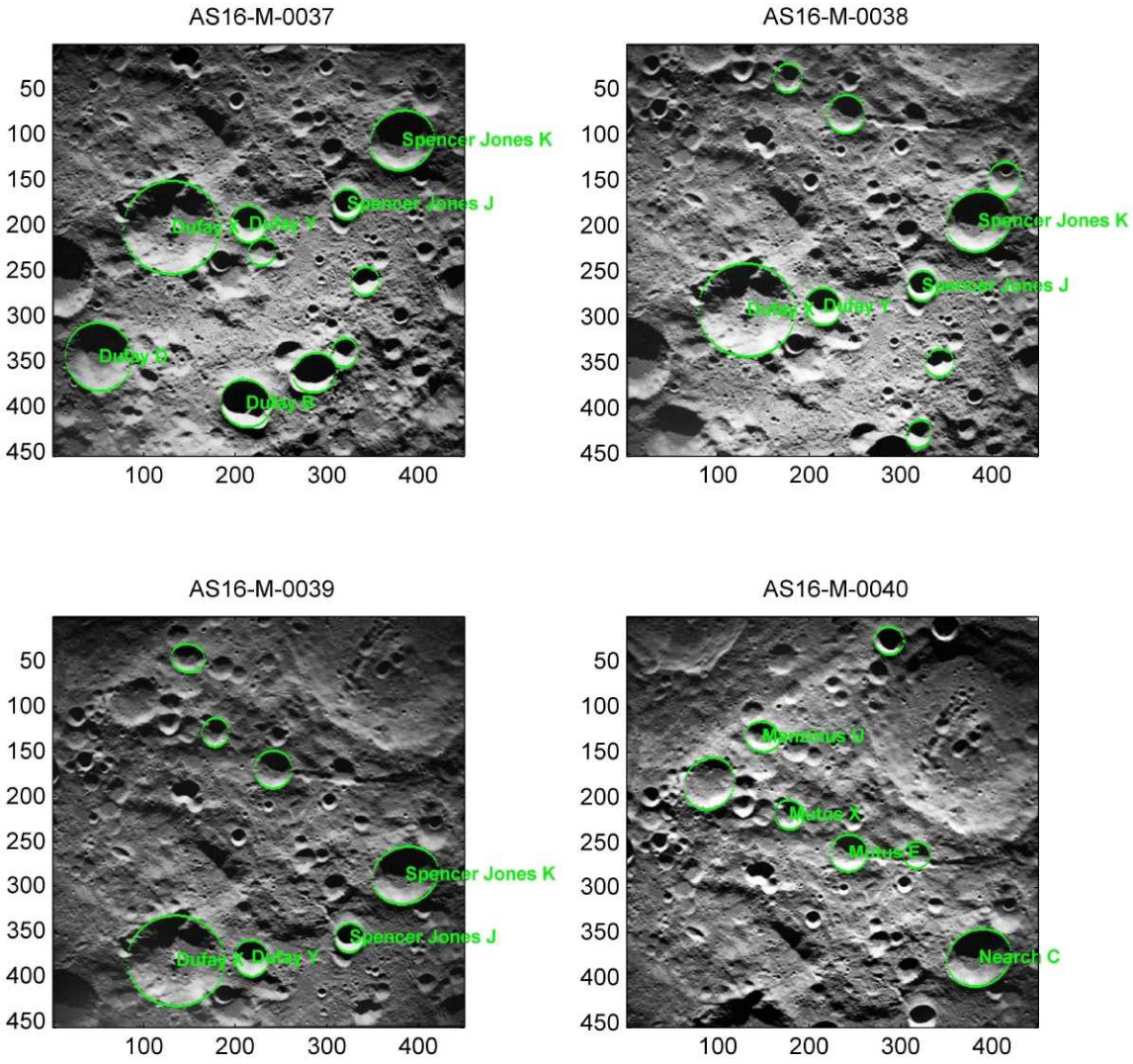

Figure 7 Crater Detection and Identification Results for Images AS16-M-0037 Through AS16-M-0040 of Apollo 16 Revolution 17 (Images Taken from[6])

Table 2 Summary of Crater Pattern Identification Results for 4 Revolutions of Apollo 16 Images With Sun Elevation Angles Between 5° and 50° (Data taken from[1])

Rev. Number	Number of Images	Number of Images with 4 or More Cataloged Craters	Number of Images with 4 or More Detected Cataloged Craters	Correctly Identified Images		Incorrectly Identified Images	
				Number Accepted	Number Rejected	Number Accepted	Number Rejected
17	73	36	24	13	3	0	16
18	69	35	19	8	5	0	16
28	72	34	14	5	3	0	16
63	72	15	0	0	0	0	18
Totals:	286	120	57	26	11	0	66

Table 3 Summary of Crater Pattern Identification Results for Images With 5 or More Detected Cataloged Craters (Data taken from[1])

Rev. Number	Number of Images with 5 or More Detected Cataloged Craters	Correctly Identified Images		Incorrectly Identified Images	
		Number Accepted	Number Rejected	Number Accepted	Number Rejected
17	11	11	0	0	0
18	8	7	1	0	0
28	9	5	1	0	3
63	0	0	0	0	0
Totals:	28	23	2	0	3

Execution Time

The execution time of the crater identification algorithm (excluding the time required for crater detection) was calculated for the processing of each image considered in revolutions 17, 18, 28, and 63. Images in which less than 4 craters were detected were not processed by the crater identification algorithm, and so were ignored for the purpose of calculating execution time. Additionally, graphical output was suppressed to provide a more accurate idea of the computational burden of the mathematical algorithm. The results are shown in Figure 8, which was generated on a Dell Latitude D830 with an Intel Core 2 Duo 2.50 GHz CPU. The mean execution time was 0.047 seconds with a standard deviation of 0.027 seconds.

The execution time of the algorithm appears to be very good, given that no *a priori* state information was provided to the algorithm (other than a the assumption of a 24 km altitude band) and the crater triangle list created from the USGS database contains 477420 crater triangles that the algorithm had to consider.

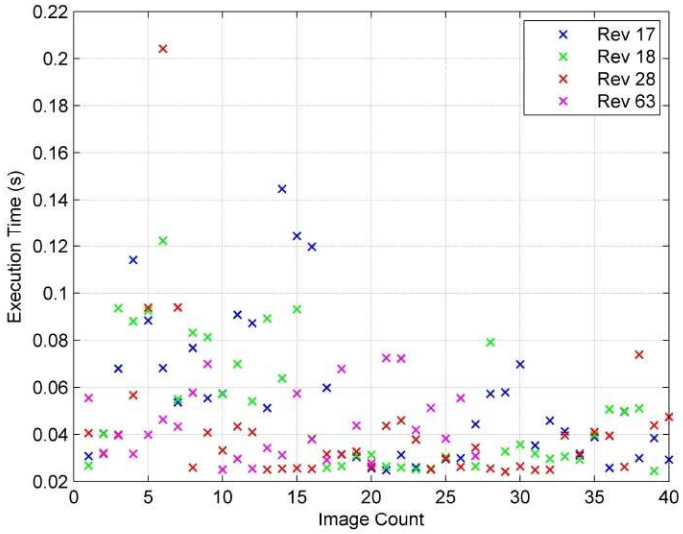

Figure 8 Execution Time of Crater Identification Algorithm on a Dell Latitude D830 with an Intel Core 2 Duo 2.50 GHz CPU; the Mean Value is 0.047 Seconds

REFERENCES

[1] Hanak, F. Chad, "Lost in Low Lunar Orbit Crater Pattern Detection and Identification," Ph.D. Dissertation, University of Texas at Austin, Department of Aerospace Engineering and Engineering Mechanics, May 2009.

[2] Leroy, B., Medioni, G., Johnson, A., and Matthies, L., "Crater Detection for Autonomous Landing on Asteroids," *Image and Vision Computing*, Vol 19, No. 11, pp. 787-792, 2001.

[3] Cheng, Y. and Ansar, A., "Landmark Based Position Estimation for Pinpoint Landing on Mars," *Proceedings of the 2005 IEEE International Conference on Robotics and Automation*, Barcelona, Spain, pp. 1573-1578, April 2005.

[4] "Gazetteer of Planetary Nomenclature," US Geological Survey Astrogeology Research Program and International Astronomical Union, *planetarynames.wr.usgs.gov/index.html*.

[5] Samaan, M. A., Mortari, D., and Junkins, J. L., "Non-Dimensional Star Identification for Un-Calibrated Star Cameras," Paper AAS 03-131 of the AAS/AIAA Space Flight Mechanics Meeting, Ponce, Puerto Rico, February, 2003.

[6] "Apollo Image Atlas," Lunar and Planetary Institute, Houston, TX, *url: www.lpi.usra.edu/resources/apollo/.*

[7] "Apollo 17 Photographic Task Requirements," *Apollo Flight Journal*, National Aeronautics and Space Administration, NASA History Division, *www.history.nasa.gov/afj.*

[8] Mortari, D., "Search-Less Algorithm for Star Pattern Recognition," *Journal of the Astronautical Sciences*, Vol. 45, No. 2, pp. 179-194, 1997.

[9] Mortari, D., Junkins, J. L., and Samaan, M. A., "Lost-in-Space Pyramid Algorithm for Robust Star Pattern Recognition," *AAS Guidance and Control Conference*, Breckenridge, CO, Feb. 10-12, 2001.

[10] Mortari, D. and Neta, B., "k-vector Range Searching Techniques," *10th Annual AIAA/AAS Space Flight Mechanics Meeting*, Paper AAS 00-128, Clearwater, FL. January 23-26, 2000.

[11] Papoulis, A., *Probability, Random Variables, and Stochastic Processes*, McGraw-Hill, Inc., New York, 1965.